applied sciences

MDPI

Article

Nitrogen Oxidation in a Multi-Pin Plasma System in the Presence and Absence of a Plasma/Liquid Interface

Moazameh Adhami Sayad Mahaleh [1], Mehrnoush Narimisa [1], Anton Nikiforov [1], Mikhail Gromov [1,*], Yury Gorbanev [2], Rim Bitar [1], Rino Morent [1] and Nathalie De Geyter [1]

[1] Research Unit Plasma Technology (RUPT), Department of Applied Physics, Ghent University, Sint-Pietersnieuwstraat 41, 9000 Ghent, Belgium; moazameh.adhamisayadmahaleh@ugent.be (M.A.S.M.); mehrnoush.narimisa@ugent.be (M.N.); anton.nikiforov@ugent.be (A.N.); rim.bitar@ugent.be (R.B.); rino.morent@ugent.be (R.M.); nathalie.degeyter@ugent.be (N.D.G.)

[2] Research Group PLASMANT, Department of Chemistry, University of Antwerp, Universiteitsplein 1, 2610 Wilrijk, Belgium; yury.gorbanev@uantwerpen.be

* Correspondence: mikhail.gromov@ugent.be

Abstract: The recent energy crisis revealed that there is a strong need to replace hydrocarbon-fueled industrial nitrogen fixation processes by alternative, more sustainable methods. In light of this, plasma-based nitrogen fixation remains one of the most promising options, considering both theoretical and experimental aspects. Lately, plasma interacting with water has received considerable attention in nitrogen fixation applications as it can trigger a unique gas- and liquid-phase chemistry. Within this context, a critical exploration of plasma-assisted nitrogen fixation with or without water presence is of great interest with an emphasis on energy costs, particularly in plasma reactors which have potential for large-scale industrial application. In this work, the presence of water in a multi-pin plasma system on nitrogen oxidation is experimentally investigated by comparing two pulsed negative DC voltage plasmas in metal–metal and metal–liquid electrode configurations. The plasma setups are designed to create similar plasma properties, including plasma power and discharge regime in both configurations. The system energy cost is calculated, considering nitrogen-containing species generated in gas and liquid phases as measured by a gas analyzer, nitrate sensor, and a colorimetry method. The energy cost profile as a function of specific energy input showed a strong dependency on the plasma operational frequency and the gas flow rate, as a result of different plasma operation regimes and initiated reverse processes. More importantly, the presence of the plasma/liquid interface increased the energy cost up to 14 ± 8%. Overall, the results showed that the presence of water in the reaction zone has a negative impact on the nitrogen fixation process.

Keywords: nitrogen fixation; plasma-based nitrogen fixation; multi-pin plasma system; plasma/liquid interface

Citation: Adhami Sayad Mahaleh, M.; Narimisa, M.; Nikiforov, A.; Gromov, M.; Gorbanev, Y.; Bitar, R.; Morent, R.; De Geyter, N. Nitrogen Oxidation in a Multi-Pin Plasma System in the Presence and Absence of a Plasma/Liquid Interface. *Appl. Sci.* **2023**, *13*, 7619. https://doi.org/10.3390/app13137619

Academic Editor: Emilio Martines

Received: 8 June 2023
Revised: 22 June 2023
Accepted: 23 June 2023
Published: 28 June 2023

1. Introduction

Nitrogen (N_2), a major constituent (78%) of the Earth's atmosphere [1], is an essential compound for the growth of plants and living organisms [2]. However, these organisms are not able to directly use nitrogen present in air, due to the high stability of the N≡N electronic configuration, which has a high dissociation energy of 9.79 eV. Within this context, nitrogen fixation (NF) is a process that provides chemical pathways to make nitrogen accessible for living organisms by converting N_2 molecules into species consumable by plants, such as NH_3 and (H)NO_x [3,4].

The beginning of the 20th century was marked by a rapid increase in nitrogen-containing fertilizers production via the Haber–Bosch (H–B) process for NH_3 synthesis [5]. The synthesis is carried out at high pressure and temperature in the presence of a catalyst, supplying nitrogen from the ambient air, together with hydrogen and energy from natural gas (CH_4) steam reforming. Such harsh operational conditions and extreme dependence

on CH_4 bring a number of significant disadvantages, namely, greenhouse gases emission (although part of the emitted CO_2 is reacted with the produced NH_3 to yield a fertilizer consisting of a solution of urea and ammonium nitrate in water, also known as UAN) and utilization of 3–5% of the total natural gas output [6]. Finally, H–B is feasible only on a large industrial scale. Considering the firm reliance of the H–B process on CH_4 and the consequent disadvantages, the need to develop and integrate a new alternative approach is of paramount importance [7].

Recently, various methods have been considered to replace (or at least to compete with) the H–B process, such as metal-complex NF, electrocatalysis, photocatalysis, thermal catalysis, and nonthermal plasma (NTP) [8,9]. Plasma is an ionized gas, consisting of ions, electrons, and noncharged species (photons, molecules, atoms, and radicals) in excited and ground states. Specifically, NTP generates an intensified plasma chemistry due to the enhanced electron temperature (T_e), while due to its nonequilibrium nature (i.e., the electron temperature and the vibrational temperature are much higher than the rotational temperature), the background gas remains closer to ambient conditions. Although electrical power is required to generate plasma, it can be supplied from renewable energy sources, providing multiple advantages of this method, namely, its compact size, making it ideal for decentralized production, its quick start-up, and its rapid response to changes in the composition of the working gas [7,10,11].

Despite the good performance of some low-pressure plasma sources [12,13], their demand to utilize vacuum systems is considered an evident disadvantage preventing industrial implementation. In contrast, considerable work is focused on developing high-pressure plasma-assisted NF processes (>1 atm) [14]. Due to its simplicity and portability, most attention is, however, paid to NF using various NTP sources operating at atmospheric pressure, including gliding arcs [15,16], corona discharges [17], plasma jets [18,19], and dielectric barrier discharges (DBDs) [20].

It must be noted that the H–B process produces NH_3, which on its own is not a fertilizer, but a fertilizer building block, and fertilizers such as UAN and NH_4NO_3 are most commonly used. Industrially, nitrates are produced via the oxidation of NH_3 via the Ostwald process [21,22]. In contrast, plasma NF largely focuses on (H)NO_x production, because it shows the most promising results in terms of energy cost and production rates. The plasma-produced (H)NO_x can be subsequently (partially) reduced to NH_3 to produce aqueous solutions of NH_4NO_3 [23,24].

In the field of plasma-based NF, the presence of water (as an electrode or as part of the gas stream) in the plasma zone has also attracted significant attention since water is considered a green hydrogen source. These discharges can generate a diversity of reactive oxygen species (ROS) and reactive nitrogen species (RNS). Using droplets in a corona discharge yielded an energy efficiency of 3.9 g/kWh for NO_x [25]. Moreover, adding water as a liquid electrode into discharge reactors also proved to be a good approach to generate aqueous nitrites and nitrates [26]. A corona discharge applied over a water surface was found to show an increase of more than 90% of NO_x transformation in HNO_2/HNO_3 compared to cases without the presence of water [27,28], thus dramatically reducing the need for downstream aqueous scrubbers to absorb the plasma-produced gaseous NO_x.

In contrast, another recent study which used a transient spark plasma demonstrated that the presence of water could induce an adverse effect by reducing the NF efficiency by approximately 20% compared to the dry air condition [29]. The divergence in the reported data between various works can be explained by an indirect comparison of the plasmas with and without water, poor plasma characterization, specifically plasma power and discharge regime, focusing only on the products generated in the gas or liquid phases. Moreover, an extensive number of studies mainly focused on miniaturized configurations and lab-scale plasma sources, and the upscaling impact is often overlooked. As such, from an industrial point of view, there is still a long way to go for plasma-assisted NF before it can be fully exploited and used as an auxiliary technology to H–B. To bridge this gap, it is

important to obtain detailed insights into plasma-assisted NF in the presence and absence of water.

The present work aims to contribute to the fundamental understanding of the impact of a plasma/liquid interface and the upscaling of the system on the energy efficiency of a plasma-assisted nitrogen oxidation process at atmospheric pressure in air. We studied plasmas generated in both multi-pin metal–metal and metal–liquid electrode configurations. First, we performed plasma diagnostics to gain insights into their power consumptions, discharge regimes, gas temperatures, and the presence of chemically reactive species, which determine the formation of stable nitrogen-containing products. Afterwards, we investigated the production of N-containing species in both the gas and liquid phases, while varying the gas flow rate and plasma power. The outcome of this fundamental study facilitates the understanding of the effect of a plasma/liquid interface in a multi-pin plasma reactor on the energy cost of the process.

2. Materials and Methods

2.1. Plasma Setup

Schemes of the used experimental setups are depicted in Figure 1. Figure 1a,b represent the schematics of two different electrode configurations under investigation, namely, metal–metal (Me–Me) and metal–liquid (Me–L), respectively. At the same time, Figure 1c illustrates a 3D representation of the setup design along with a photograph of the plasma observed from the optical window. The DC voltage output of the main power supply (Technix 30 kV, 40 mA) was transferred into a pulsed voltage and distributed along 14 pins using the so-called chopping gap method, as described elsewhere [30,31]. The details about the electrical circuit used in this work are presented in the Supplementary Information (SI). The reactors studied in this work can be easily scaled up by increasing the number of pins and the applied power to any desirable value.

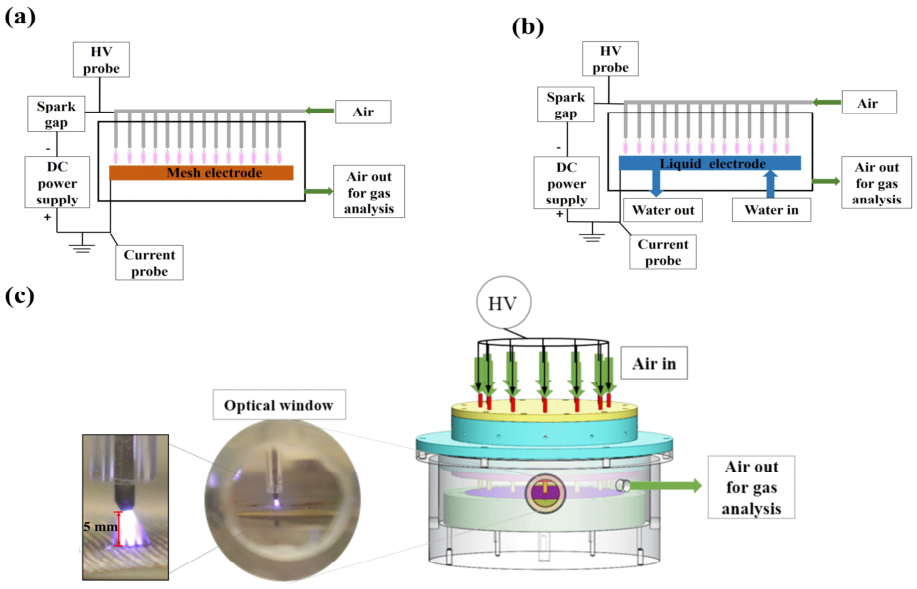

Figure 1. Schematic representations of the experimental setups in (**a**) metal–metal and (**b**) metal–liquid electrode configurations, and (**c**) a 3D representation of the reactor together with a photograph of one pin while the plasma was operational.

The reactor in the pin-to-plate configuration consisted of 14 pins inserted inside quartz tubes and used as high voltage electrodes. The supplied gas distribution network was designed in such a way to ensure an equal distribution of air coming into the plasma zone and to control the gas residence time. In both systems, dry air (Air Liquide-Alphagaz 1, 99.9% purity) was used as operational gas with a gas flow rate of 4, 6, 8, 10, and 12 standard liters per minute (L min^{-1}). The Me–Me setup configuration used a circular stainless steel

mesh plate of 12 cm diameter (opening of 200 μm and a thickness of 150 μm) as grounded electrode. In the Me–L system, a sodium dihydrogen phosphate (NaH_2PO_4, Carl Roth GmbH + Co, 98%) solution in water with a conductivity of σ = 350 μS/cm was used as a liquid electrode instead of the mesh plate electrode. The water solution was pumped into the system at a liquid flow rate of 20 mL min^{-1}, enabling a stable liquid level with a volume of 11.3 cm^3 in the chamber, which possesses a volume of 971.5 cm^3. At the same time, the increased conductivity ensured a stable plasma operation. The discharge gap was fixed at 5 mm for both investigated configurations during all experiments.

2.2. Plasma Diagnostic Methods

2.2.1. Electrical Characterization

Electrical characterization of the plasmas was performed to ensure that both Me–Me and Me–L reactors could operate within the same power range. For this, the plasma voltage and current waveforms were recorded via an oscilloscope (LeCroy WaveRunner 64Xi, 600 MHz bandwidth, LeCroy, Chestnut Ridge, NY, USA), employing a high-voltage probe (P6105A, 75 MHz bandwidth, Tektronix, Beaverton, OR, USA) and current transformer (Pearson Current Monitor: model 2877, Pearson Electronics Inc., Palo Alto, CA, USA). Afterwards, the plasma power was calculated as follows:

$$P = f\int_0^T V(t) \times I(t)dt, \quad (1)$$

where V(t) and I(t) are instantaneous voltage and current, respectively, while f is the voltage frequency defined by the charge–discharge rate of the capacitor in the chopping gap electrical schematic (see Figure S2 for more details). In addition, the number of plasma strikes that appeared within one period was determined from the current–voltage waveforms, filtering all current peaks with threshold height above 10%.

2.2.2. Optical Emission Spectroscopy

The gas temperature (T_{gas}) is an important plasma characteristic that defines the reaction rate of the occurring chemical processes. In nonequilibrium plasmas, it is a widely accepted approximation that rotational and translational (gas) temperatures are assumed to be in equilibrium due to the fast rotational–translational energy transfer, taking place within less than 1 ns at atmospheric pressure [32]. Since N_2 is the dominant component in the used gas, the gas temperature was measured by recording the emission signal originating from the second positive system of N_2 (N_2 ($C^3\Pi_u$ – $B^3\Pi_g$)). Accordingly, optical emission spectroscopy (OES) was performed employing high-resolution spectrometers (Horiba, iHR550, Horiba Ltd., Kyoto, Japan with 1200 gr/mm grating and FC-UVIR600-2, Avantes, Apeldoorn, The Netherlands) with UV-VIS optical fiber and a collimating lens, which were placed in front of the fused silica window located in the outer wall of the plasma reactor, as shown in Figure 1c. Nitrogen transitions in the wavelength range 300–385 nm were recorded, and the gas temperature was obtained, matching the simulated and experimental spectra via Massive OES software [33,34]. An example of a fitted spectrum is shown in the SI, Figure S3. In this work, time and spatially averaged measurements were carried out, meaning that the temperatures determined via this approach correspond to the plasma core region. Additionally, OES in the optical range of 200–900 nm were also recorded using a broad band, low resolution spectrometer (Ocean Optics S2000, 1.4 nm spectral resolution, Duiven, the Netherlands) to monitor the differences in plasma composition between Me–Me and Me–L configurations based on the emission signal from electronically excited states. All measured spectra were calibrated using a standardized tungsten halogen lamp (Oriel: model 63355, 250–2400 nm optical range, MKS Instruments Inc., Irvine, CA, USA).

2.2.3. Electron Density

The electron density (n_e) is the primary plasma parameter describing the discharge operation regime (pulse corona 10^8–10^{11} cm^{-3} > transient glow 10^{12}–10^{13} cm^{-3} > streamer

10^{14}–10^{15} cm^{-3} > spark 10^{16}–10^{18} cm^{-3}) [35,36]. In this work, n_e was determined using the current–voltage method utilizing the measured electrical characteristics and plasma geometry as described elsewhere [37]. For this, the electrical field strength (E/N) was estimated using the measured voltage and the discharge gap, while the neutral particles density (n) was calculated, considering T_{gas} measured via OES as follows:

$$n = \frac{P}{kT_{gas}}, \quad (2)$$

In Equation (2), P is the gas pressure, and k is the Boltzmann constant. Accordingly, n_e was estimated as

$$n_e = \frac{J}{ev_e\frac{E}{N}} = \frac{J}{eE\mu_e}, \; J = \frac{I}{S} \quad (3)$$

where J is the current density in $A.m^{-2}$, S is the cross-section of the discharge in m^2, e is the elementary charge in C, E is the electrical field in $V{\cdot}m^{-1}$ (calculated experimentally), v_e is the electron drift velocity in m s^{-1}, and μ_e is the electron mobility in $m^2{\cdot}Vs^{-1}$. J was calculated, considering a streamer diameter of 150 µm [38], while the electron mobility was estimated using a BOLSIG+ solver [39].

2.3. NO_x Detection in the Gas and Liquid Phases

After passing through the plasma reactor, the gas composition was examined using a gas analyzer system (Testo 350, Testo SE & Co. KGaA, Titisee-Neustadt, Germany), allowing us to observe NO and NO_2 species in the range of 0–5000 ppm with an accuracy of 5 ppm. For this purpose, the gas analyzer was connected in series with the plasma reactor outlet. In the case of the Me–L electrode configuration, liquid samples of 2 mL were collected after 15 min of plasma exposure, and the nitrite (NO_2^-) and nitrate (NO_3^-) concentrations produced in the liquid phase were measured employing two different methods. The NO_2^- concentration was determined using the Griess assay, a standardized method for examining water and wastewater [40,41]. The Griess reagent was prepared according to the procedure described in the SI. Meanwhile, the NO_3^- concentration was quantified employing a Nitrate 3021 combination ion selective electrode immersed into a plasma-exposed liquid sample. All gas and liquid phase measurements were carried out in triplicate. It is worth noting that the gas treatment time for the Me–Me system was kept consistent with that of the water system, ensuring uniformity in the measurements.

2.4. Calculation of Specific Energy Input and Energy Cost

The final comparison of the two plasma systems with and without water presence investigated in this work was performed in terms of specific energy input (SEI) to distinguish the effect of varying gas flow rate and in terms of energy cost (EC) to compare the effectiveness of the Me–Me and Me–L plasmas. Within this context, the SEI was calculated as follows:

$$SEI(J/L) = \frac{P(W)}{Q\left(L\ min^{-1}\right)} \times 60(s\ min^{-1}) \quad (4)$$

where Q is the gas flow rate and P the power. The EC was calculated using the following equation:

$$EC_{N-fixed}[MJ/mol] = \frac{P[W]}{\text{moles of fixed N produced per second } [mols^{-1}]} \cdot \frac{1}{10^6[\frac{J}{MJ}]} \quad (5)$$

considering nitrogen-containing products formed in the gas (NO, NO_2) and liquid (NO_2^-, NO_3^-) phases, as described in more detail in the SI.

3. Results and Discussion

3.1. Plasma Diagnostics

To compare the energy efficiency of NF in the Me–Me and Me–L electrode configurations, it is crucial to ensure that both systems operate at identical conditions. Therefore, plasma diagnostics were first carried out to determine the plasma powers, discharge regimes, corresponding gas temperatures, and to identify the reactive plasma species in both reactor configurations. It is worth noting that the experimental results obtained for different gas flow rates were compared and consistent trends were noted within the studied range of gas flow rates. Therefore, the article presents only the data for the gas flow rates of 4, 8, and 12 L min^{-1} for clearer data visualization. The rest of the data can be found in the SI.

A typical current–voltage characteristic recorded after the spark gap is shown in Figure 2a, while this figure's inset shows a zoom-in of the time period when a main plasma pulse occurs. Under this condition, the discharge power was calculated to be 20 ± 2 W, and the peak current reached 11 A. It is important to note that such current values normally correspond to streamer or spark plasmas [42]. Meanwhile, an increase in the applied DC voltage (and thus an increase in plasma power) and the gas flow rate results in a more frequent formation of voltage pulses from 40 up to 250 Hz, as shown in Figure 2b, independently from the electrode configurations. This leads to a higher number of discharges (current peaks) observed within one period (from 1 at 20 W to 100's at 90 W). The same trend can also be observed from the time-averaged plasma images shown in Figure 2c, where at 20 W, the plasma represents a single filament; while reaching 90 W, the number of filaments significantly increases, concentrating in the middle of the plasma gap. In addition, based on the images shown in Figure 2c, the plasma volume shows a 15 times increase when increasing the plasma power from 20 to 90 W, indicating a nonlinear increase in the plasma-treated gas volume. The plasma volume and number of discharges should strongly impact the overall plasma-triggered chemistry via a higher collision possibility between reactant molecules and electrons. Finally, Figure 2d shows the plasma power as a function of the parameter VA (applied power) averaged over all flow rates under investigation. This result illustrates that both plasma systems with and without water presence operate within the same power range, showing the similarity in electrical properties, thereby allowing their direct comparison.

OES was employed to determine the difference in the gas phase compositions as well as the gas temperatures in the Me–Me and Me–L setup configurations. First, the emission spectra in a wide wavelength range from 200 to 900 nm were recorded, and an example of the observed spectra is shown in Figure 3. The spectra for the Me–Me and Me–L electrode arrangements repeat each other well and illustrate emissions from the first positive system of N_2 ($N_2\left(B^3\Pi_u \rightarrow A^3\Sigma_u\right)$), the second positive system of N_2 ($N_2\left(C^3\Pi_u \rightarrow B^3\Pi_g\right)$), and the first negative system of N_2^+ ($N_2^+\left(B^2\Sigma \rightarrow X^2\Sigma\right)$) [40]. However, a clear difference between the two plasma systems is observed in the wavelength range from 300 to 315 nm, indicating the presence of the OH$\left(A^2\Sigma^+ \rightarrow X^2\Pi\right)$ rotational band in the case of the liquid electrode, which can be more clearly seen from the high-resolution spectrum in the inset of Figure 3. These OH radicals originate from the dissociation of water available in the Me–L system. The presence of water in the gas phase is a result of plasma/liquid interactions, leading to water evaporation and decomposition into OH and H, which contributes to the OH radical emission [43,44]. It is noteworthy to mention that the OES spectra obtained at different plasma powers and different gas flow rates are very similar in terms of observed emission lines, indicating that similar radiative excited plasma species are present under all investigated conditions.

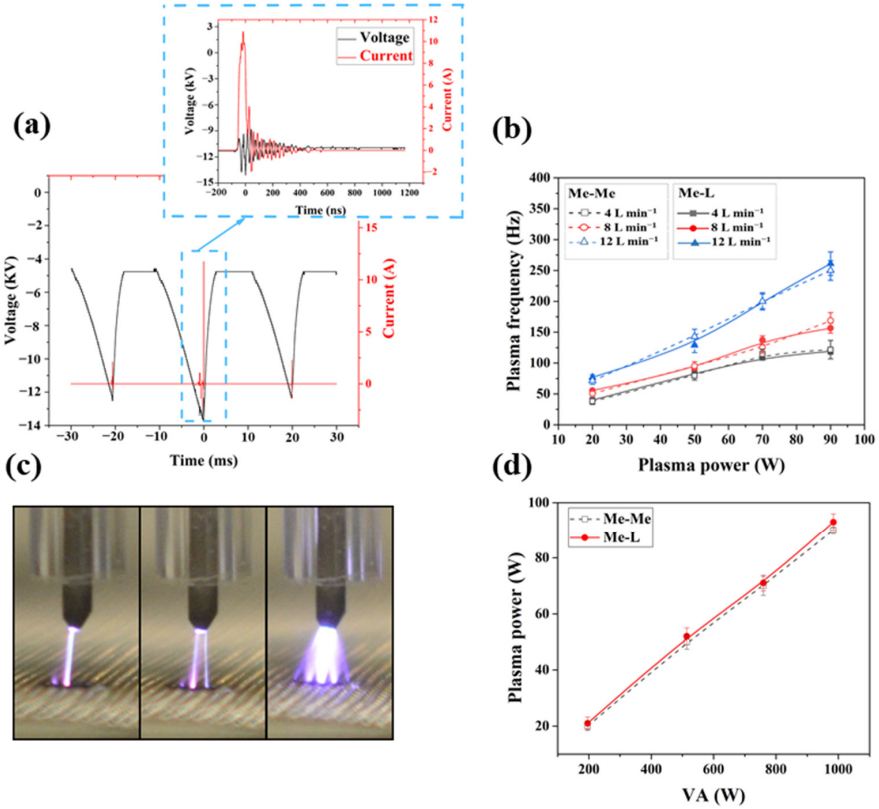

Figure 2. (**a**) An example of current–voltage waveforms in the Me–Me electrode configuration measured for a gas flow rate of 4 L min^{-1} and a plasma power of 20 ± 2 W with an inset showing a zoom-in of the main plasma pulse. (**b**) Plasma frequency in the chopping gap as a function of plasma power for different air flow rates. (**c**) Examples of plasma images at 4 L min^{-1} flow rate and plasma power of 20, 50, and 90 W with plasma volumes of 2.7 ± 0.1, 4.7 ± 0.6, and 39.5 ± 3 mm^3, respectively, after an exposure time of 5 ms. (**d**) Plasma power averaged over all gas flow rates in the Me–Me and Me–L setup configurations versus applied power.

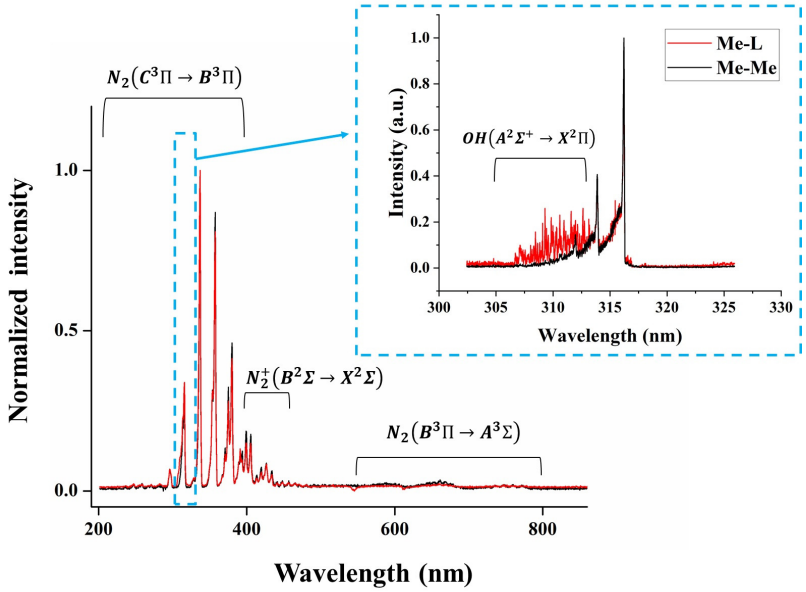

Figure 3. Optical emission spectra of the plasmas in the Me–Me and Me–L electrode configurations at a gas flow rate of 4 L min^{-1} and a discharge power of 90 ± 2 W.

In addition to a qualitative analysis of the excited plasma species, quantitative studies of the gas temperature were conducted via OES. Figure 4a represents T_{gas} in the Me–Me and Me–L configurations as a function of plasma power for gas flow rates of 4, 8, and 12 L min^{-1} (the results for all flow rates under investigation are shown in the SI, Figure S5). As can be seen, the Me–L system always shows a higher gas temperature compared with the Me–Me system at all gas flow rates and plasma powers ($\Delta T_{gas} \approx 433 \pm 30$ K). This can be attributed to an increase in the H_2O content in the plasma zone, which has higher vibrational–vibrational (V–V) and vibrational–translational (V–T) relaxation rates than N_2 and O_2, resulting in a fast gas heating and plasma thermalization [45,46]. At the same time, a decrease in gas temperature is observed with increasing gas flow rate for both plasma systems, as illustrated in Figure 5b. From the literature, it is well known that one of the mechanisms to sustain plasma and prevent it from the so-called streamer-to-spark transition, avoiding undesirable energy losses on gas heating and plasma constriction, is to increase the gas flow rate [47]. Therefore, the decrease in the gas temperature with gas flow rate can be prescribed to the same phenomena, which leads the plasma back to the streamer mode. In addition, it is essential to note that the gas temperature measured via this method represents the temperature inside the plasma filament (the region with the highest emissivity). Therefore, considering that the number of plasma pulses and the plasma-treated gas volume increase with plasma power, it can be concluded that the overall gas volume between the two electrodes could be heated significantly. Overall, this all has to be considered when evaluating the final EC of the processes.

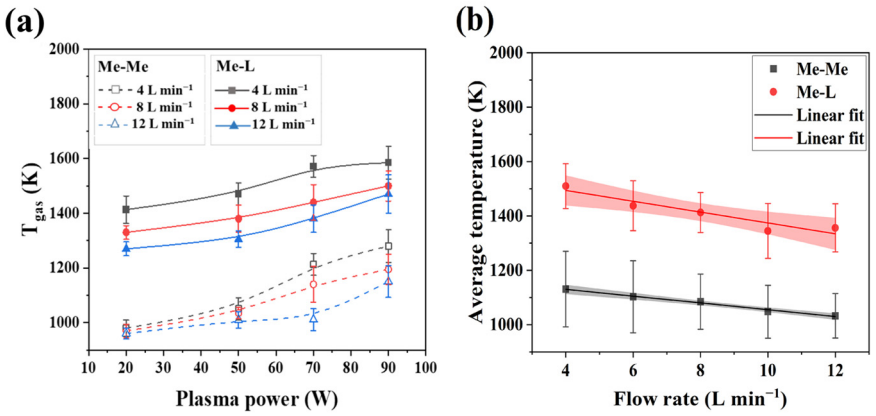

Figure 4. (**a**) The gas temperature estimated via OES for different gas flow rates as a function of plasma power. (**b**) The average gas temperature over the plasma power range under investigation as a function of gas flow rates.

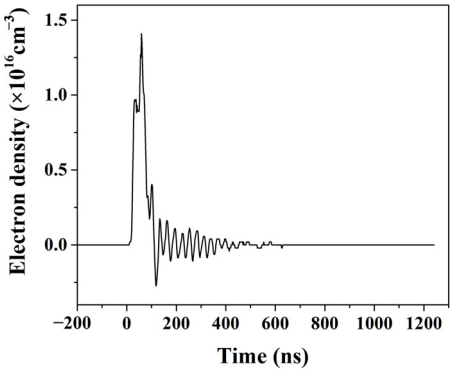

Figure 5. Electron density profile for a single current peak at a flow rate of 4 L min^{-1} and a plasma power of 20 ± 2 W in the Me–Me system.

Electron density (n_e) is one of the main plasma characteristics determining plasma physical properties, namely, the ionization degree (~plasma regime). In this work, n_e was estimated to reveal the discharge operational regimes, employing the current–voltage method and considering a plasma channel diameter of 150 µm [48,49]. Figure 5 shows an example of the time-resolved n_e evolution for the main current peak in the Me–Me system at a plasma power of 20 ± 2 W, a gas flow rate of 4 L min^{-1}, and T_g of 1000 K. Under this experimental condition, the peak electron density reaches $1.4 \times 10^{16} \pm 0.2 \times 10^{16}$ cm^{-3} and follows the structure of the current profile. Following the same approach, n_e was calculated for all experimental conditions, and the results are shown in the SI, Figure S6. It was found that n_e shows relatively constant values in both Me–Me and Me–L reactor configurations and varies between $1.2–2.1 \times 10^{16} \pm 0.4 \times 10^{16}$ cm^{-3} and $0.8–2.4 \times 10^{16} \pm 0.2 \times 10^{16}$ cm^{-3}, respectively. These values correspond well to the so-called transient spark mode where a plasma is typically initiated by a streamer, followed by a short (~100 ns) high current (~10 A) pulse. In this case, the transition to a "full" spark discharge is limited by the voltage duration [36]. However, the used method is highly sensitive to the plasma channel diameter and strongly depends on the gas phase composition. Therefore, considering possible errors of the used method, it is hard, if even possible, to make a conclusion about the n_e behavior at different gas flow rates and plasma powers.

To summarize, it can be stated that the interchange between the metal and the liquid ground electrodes has a negligible impact on plasma power and discharge mode. However, the plasma power is directly proportional to the number of plasma filaments and the plasma volume (higher power → more filaments → higher plasma volume). OES indicates that the main difference between the Me–Me and Me–L reactors is the presence of OH radicals in the latter case. Moreover, the gas temperature measurements show that the presence of a plasma/liquid interface results in plasma thermalization (although only of ~400 K) that might have a negative cause on plasma-based nitrogen fixation energy efficiency. The following section is dedicated to the determination of the produced stable nitrogen-containing products in both gas and liquid phases.

3.2. Nitrogen Fixation Process

3.2.1. Gas Phase Products

The NF pathways toward nitrogen oxides formation were already comprehensively investigated elsewhere [50–52]. This work therefore only intends to give a brief overview of the NF kinetics, considering the species generated in the plasma. The reactions discussed within this study together with their reaction rate constants are summarized in the SI, Table S1.

In the gaseous phase of an air plasma, NO radicals are preliminary species formed via the so-called Zeldovich mechanism [53,54]. Under nonequilibrium plasma conditions, the main driving force in this mechanism is molecular nitrogen excited states, including electronically and vibrationally excited nitrogen molecules. Simplified reactions are shown in the reactions below:

Reaction (1):

$$N_2 + O \rightarrow NO + N$$

Reaction (2):

$$N + O_2 \rightarrow NO + O$$

However, in the presence of water, this mechanism can be extended by a third reaction involving OH radicals, which are one of the main products resulting from water dissociation:

Reaction (3):

$$N + OH \rightarrow NO + H$$

Reactions (1)–(3) are also known as the extended Zeldovich mechanism, where Reaction (3) has a reaction rate constant of approximately one order of magnitude higher than Reaction (2). In turn, OH radicals are mainly generated through reactions with electronically excited oxygen atoms, molecular nitrogen, and via direct electron dissociation, as presented in Table S1. This means that the energetic species generated by plasma can be spent differently depending on the gas composition, and it is difficult to predict which mechanism is more efficient without solving (at least) a 0-D computer model.

In a next step, the produced NO can be oxidized to form NO_2 as follows [55,56]:

Reaction (4):

$$NO + O_3 \rightarrow O_2 + NO_2$$

However, Reaction (4) requires the presence of ozone which is not stable at high temperatures, as is the case in this work [57]. Under this condition, other pathways resulting in NO_2 generation can be as follows:

Reaction (5):

$$NO + O \rightarrow NO_2$$

Reaction (6):

$$2NO + O_2 \rightarrow 2NO_2$$

Considering these mechanisms, the plasma outlet gas was monitored for the presence of NO and NO_2 species. The results are shown in Figure 6 for both Me–Me and Me–L configurations as a function of SEI for gas flow rates of 4, 8, and 12 L min^{-1} (the results for all flow rates under investigation are shown in the SI, Figure S7). According to the series of graphs illustrated in Figure 6, both NO and NO_2 concentrations increase with increasing SEI. Indeed, a higher power leads to an increase in SEI, and, thus, a higher number of energetic electrons. These electrons collide with carrier gas molecules (N_2 and O_2), forming energetic species, e.g., electronically or vibrationally excited states, which contribute to NO and NO_2 formation [28]. Interestingly, the curves show an identical behavior across all experimental gas flow rates. This observation suggests that the mechanisms through which NO_x species are being generated are independent of the used gas flow rates. It is also worth mentioning that the NO_x formation in both systems for all investigated gas flow rates more rapidly increases for SEI values higher than 1000 J/L compared to its increase at lower SEI values. This can be attributed to the more often plasma streamer appearance and the increase in plasma-treated gas volume at higher SEI values, indicating a shift in the occurring plasma-based nitrogen fixation chemical kinetics. At high SEI values, the high plasma frequency promotes the formation of reactive species that can trigger reverse processes, causing a decrease in NO_x formation, as was already shown elsewhere [51]. At the same time, as already mentioned in Section 3.1, the rise in the number of plasma streamers could significantly heat the gas volume between the electrodes. This can in turn promote thermal nitrogen fixation and/or increase the rate of the occurring chemical reactions. This suggestion is also supported by the most pronounced change in the curve slope measured at a gas flow rate of 4 L min^{-1} (Figure 6), where the gas temperature in the plasma core is the highest and the gas residence time is the lowest.

Figure 6 also shows slightly lower concentrations of NO and NO_2 in the Me–L setup configuration compared to the Me–Me system. This observation is most likely due to the fact that a certain amount of NO_x species are absorbed in the liquid phase. This effect is more pronounced for NO_2 species and can be explained considering that the Henry constant of NO_2 is higher than for NO. The latter results lead to the conclusion that nitrogen-containing products in the liquid phase should be further evaluated, which is the focus of the following section.

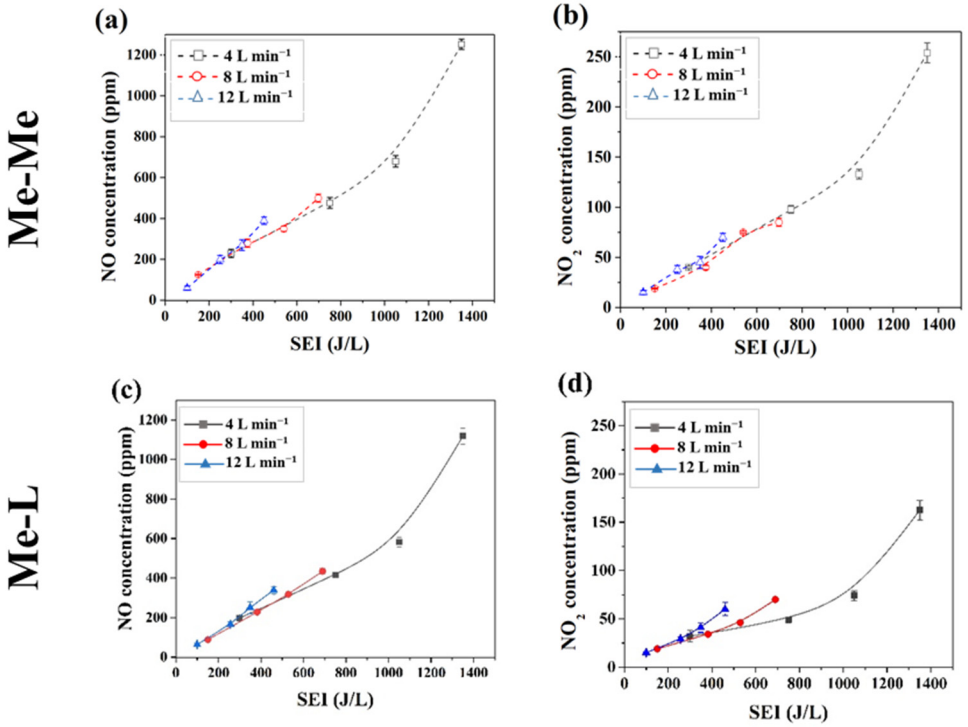

Figure 6. (**a**,**c**) NO and (**b**,**d**) NO_2 concentrations as a function of SEI for different gas flow rates for both the Me–Me and Me–L systems.

3.2.2. Liquid Phase Analysis

Based on Henry's law, the gas phase NO_x products can penetrate into the aqueous phase, interact with H_2O, and form NO_2^- and NO_3^- as follows:

Reaction (7):

$$2NO_2 + H_2O \rightarrow NO_2^- + NO_3^- + 2H^+$$

Reaction (8):

$$NO + NO_2 + H_2O \rightarrow 2NO_2^- + 2H^+$$

Reaction (9):

$$2NO + O_2 + H_2O \rightarrow 2NO_2^- + 2H^+$$

Reaction (10):

$$NO + NO_2 + H_2O \rightarrow 2NO_2^- + 2H^+$$

Consequently, the combined concentrations of NO_2^- and NO_3^- in the liquid phase correspond to the total amount of NO_x converted into HNO_x species which remain dissolved in the liquid. The NO_2^- and NO_3^- concentrations in the liquid phase have been evaluated in this study and the results are presented in Figure 7 as a function of SEI for different applied gas flow rates (the same profiles for all flow rates under study are shown in the SI, Figure S8). We also acknowledge that, according to recent studies, in both plasma-catalytic and catalyst-free systems, air plasma with added water can generate NH_3 [27,58,59]. However, the selectivity to NH_3 generation is dramatically lower than to (H)NO_x generation, typically leading to very small amounts of NH_3. Interestingly, NH_3 production in a humidified air plasma has recently been reported [27]. However, in our case, plasma was discharging onto liquid water, and, furthermore, we did not observe any NH emission by OES. Hence, we believe that NH_3 may be formed in our Me–L system, but most likely only in negligible amounts. Consequently, we believe that evaluating solely (H)NO_x species as NF products is sufficient for the discussion in the present work.

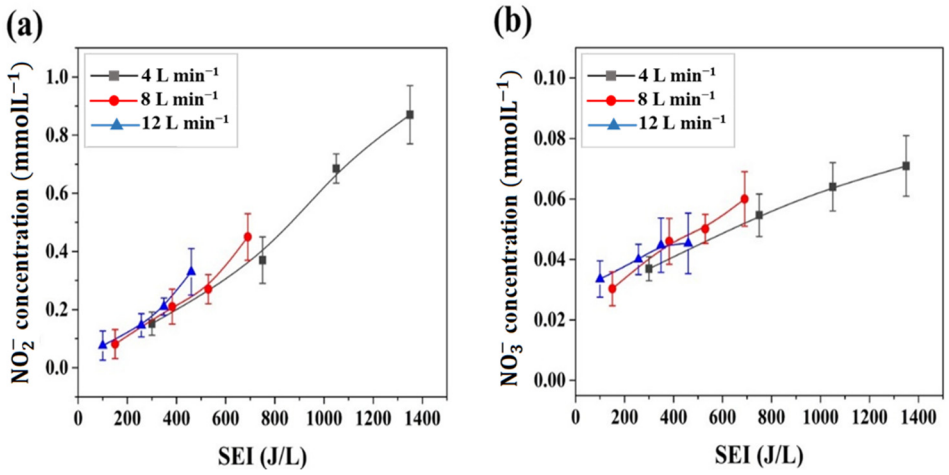

Figure 7. Evolution of (**a**) nitrite and (**b**) nitrate concentrations generated in the liquid phase as a function of SEI at different gas flow rates in the Me–L system.

It is also important to mention that in order to effectively utilize these products (NO_x) initially produced in the gas phase as fertilizer, they must be fully dissolved in a liquid to form NO_3^- as the final valuable chemical. As indicated by the reactions in Table S1, in the presence of liquid H_2O, NO_x species undergo transformation resulting in NO_2^- and NO_3^- generation. In the presence of air and sufficient contact time with O_2, all NO_2^- is converted into nitrate NO_3^-, which is already a fertilizer. In addition, this work focuses only on the oxidation pathways of nitrogen fixation; however, literature reports suggest that even in air plasmas with H_2O, some NH_4^+ generation occurs [27]. To increase the fraction of NH_4^+, some nitrates accumulated in the liquid can be reduced (e.g., electrochemically) into NH_3. This essentially creates a solution of NH_4NO_3, the most widely used fertilizer [27,59]. Thus, following this approach, the fertilizer can be produced directly on-site without transportation expenses and with no requirement to separate the fertilizer from the solution.

Identical to NO and NO_2 (Figure 6c,d) in the Me–L system, for each of the gas flow rates under study, the concentrations of nitrite and nitrate increase with increasing SEI. The results also reveal that the Me–L system mainly promotes the production of NO_2^-, as for each experimental condition its concentration was almost one order of magnitude higher compared to NO_3^-. This can be attributed to the fact that H_2O_2 (the main oxidant converting NO_2^- to NO_3^- [60]) is only formed in very minor amounts. Finally, all measured points for different gas flow rates are within the error bar range, which reveals that the applied gas flow rate only has a very minor effect on the NO_2^- and NO_3^- concentrations produced in the liquid phase. This can be ascribed to the specific geometry of the setup where the supplied gas does not pass through the liquid.

In general, when comparing Figures 6 and 7, it can be concluded that the concentration of stable nitrogen-containing compounds increases similarly with SEI in both plasma systems. However, the liquid phase analysis clearly demonstrates that the concentration of NO_x^- species is significant and must be considered when evaluating the energy cost of plasma-based nitrogen fixation in the presence of water.

3.3. Energy Cost of the Nitrogen Fixation Process in the Multi-Pin System with and without Water

The final evaluation of the Me–Me and Me–L systems is performed in terms of energy cost (EC) of the fixed nitrogen molecule, considering all detected nitrogen-containing species in gas and liquid phases. The EC profiles of plasma-assisted NF in the Me–Me and Me–L configurations are presented in Figure 8a for gas flow rates of 4, 8, and 12 L min^{-1}, while the results for other investigated gas flow rates can be found in the SI, Figure S9. All EC curves presented in Figure 8a have a similar shape, passing through a well-defined maximum. This behavior can be explained by dividing the EC profiles into three distinct

regions, as shown in the inset of Figure 8a. Here, region I, which is characterized by an almost linear increase in EC with increasing SEI values, represents the SEI range where the increase in the number of plasma filaments promotes the reverse reactions, leading to the formation of the initial products, namely, N_2 and/or O_2, reducing the energy efficiency of the NF process. The same conclusion was made in [52], investigating the N_2-oxidation kinetics at similar conditions. Region II shows the SEI range where the formation and loss reactions of NF are equilibrated. Lastly, region III, showing a sharp decrease in EC with increasing SEI, can be attributed to the significant, nonlinear increase in the number of plasma discharges, meaning a higher gas conversion. At the same time, this plasma behavior can escalate the overall gas temperature in the gap (see Section 3.1 for more details), providing an additional boost in reaction rates and an additional chemical pathway through which nitrogen fixation can proceed, particularly thermal-driven mechanisms. This all shows that the plasma frequency strongly impacts plasma-assisted NF and that an optimal balance between plasma frequency and gas residence time must be found to reach a minimal EC. An additional point toward this conclusion is the behavior of the EC curves at different gas flow rates. As shown in Figure 8a, the EC of the process within region I increases with the gas flow rate. This correlates with the high discharge frequency at a higher gas flow rate (see Figure 2b) that triggers reverse processes, as discussed above. However, a pronounced reduction in EC values at the end of region III at the same SEI but different gas flow rates (e.g., the EC at 450 (J/L) in the Me–Me system is 28, 29, 23.5 MJ/mol for 4, 8, and 12 L min^{-1}, respectively) underlines the best balance between gas residence time and plasma frequency. Literally, this means that a higher gas flow rate brings an additional cooling effect, suppressing the reverse processes.

It is worth noting that although the EC of the process is considerably low at both low and high SEI values for all studied gas flow rates, the production rate of NF products increases significantly with an increase in SEI, as shown in Figure 8b. For example, in the Me–L system, with a flow rate of 4 L min^{-1}, the EC is approximately 27 MJ/mol and 23 MJ/mol at an SEI value of 300 and 1400 J/L, respectively, which are very similar EC values. However, when looking at the production rate at these two SEI values, an increase of nearly 13 times could be observed in the production rate (from 1.0 to 13.4 mmol/h, as marked in Figure 8b). This clearly indicates that a high production rate can be achieved in combination with a low EC, which is possible in region III of the EC profile.

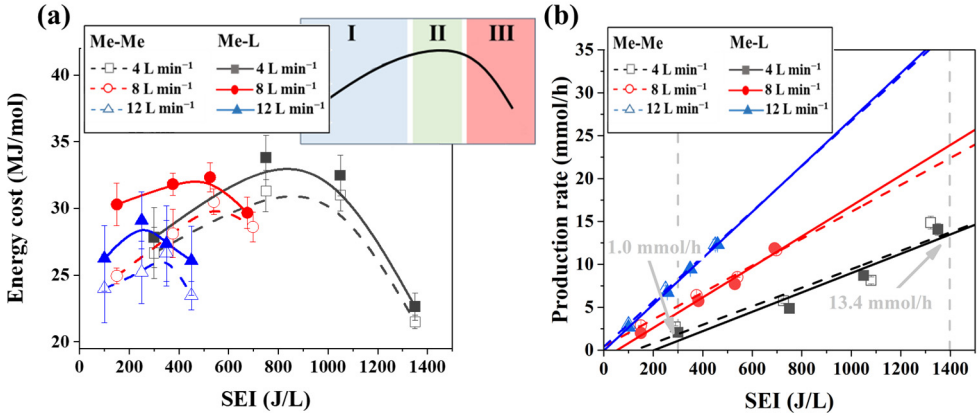

Figure 8. (**a**) Energy cost and (**b**) production rate of the NF product in the Me–Me and Me–L configurations for different gas flow rates.

Finally, when comparing the EC plots of the NF process with (Me–L system) and without (Me–Me system) water presence (Figure 8a), it becomes evident that the water electrode has a negative impact on nitrogen oxide formation, reducing it by 14 ± 8% (on average) at different gas flow rates and SEIs. This can only be explained by the energy losses during H_2O dissociation and/or evaporation and means that the extended Zeldovich mechanism Reactions (1)–(3) over the liquid electrode is less efficient compared to the

Zeldovich mechanism Reactions (1) and (2) in nonequilibrium plasmas. Moreover, an elevated gas temperature of plasma streamers in the case of the Me–L system ($\Delta T_g \approx 400$ K) is also a good representative of the additional energy losses on gas heating. It is noteworthy that a similar reduced energy efficiency of plasma-based nitrogen fixation in the presence of water was also previously reported by Gromov et al. (20 ± 6%) [23]. However, the latter investigation was dedicated to a single-pin (lab-scale) setup, operating within restricted plasma power (<20 W) and gas flow rate (<3 L min^{-1}) ranges. Nevertheless, the similarity in occurring EC reductions clearly shows that the use of a liquid electrode does not improve the performance of NF process.

To summarize, plasma-assisted NF was studied with (Me–L) and without (Me–Me) the presence of water in a multi-pin electrode system in this work. The comparison between both plasma configurations showed that the NF process is very sensitive to the plasma operational conditions, namely, the plasma frequency and the gas residence time. An increase in the appearance of plasma events per second (approximately <100 Hz) can trigger reverse nitrogen fixation processes, leading to the "back" formation of feedstock gas components (N_2 and O_2). On the other hand, a significantly high plasma frequency (>100 Hz) can promote a thermal effect, increasing the reaction rates of the occurring chemical processes and making thermal-driven nitrogen fixation more dominant. In addition, using a higher gas flow rate increases the production rate of nitrogen-fixed products. Finally, the presence of water in the plasma zone has a negative effect on plasma-assisted nitrogen fixation, resulting in an elevated energy cost. However, in a hypothetical process of nitrogen fixation and subsequent generation of fertilizers, the plasma-generated NO_x would have to be absorbed by an aqueous scrubber placed in line with a plasma reactor. In this way, NO_x^- can accumulate in the liquid and be transferred to the final fertilizer.

4. Conclusions

This work is dedicated to a fundamental study of plasma-assisted nitrogen fixation towards nitrogen oxides formed in the absence and presence of a plasma/liquid interface, evaluating the effect of a multi-pin plasma reactor driven by a pulsed DC voltage. Metal–metal (Me–Me) and metal–liquid (Me–L) electrode arrangements were compared regarding their energy costs to fix nitrogen molecules within a broad specific energy input range. To obtain insights into NF, we first studied the physical properties of the investigated plasma setups via several plasma diagnostic techniques. Through the investigation, the sustainability of plasmas under various air flow rates was observed. It was evident that plasmas were sustained in different air flow rates of 4, 6, 8, 10, and 12 L min^{-1}. They all operated within an identical power range (from 20 to 90 W), indicating a consistent behavior of the plasmas regardless of the air flow rate applied. The plasmas exhibited a transient spark regime with an electron density of 10^{16} cm^{-3}. Furthermore, it was observed that the plasma frequencies varied within a wide range from 1 to 100's of Hz. In addition, the Me–L system showed a higher gas temperature (increase by 400 K) in the core of the plasma streamer. In both the Me–Me and Me–L configurations, the nitrogen-fixed products were evaluated in the gas and liquid phases and the configurations were compared in terms of energy cost per fixed N_2 molecule. Analysis revealed that the nitrogen fixation process is strongly dependent on the plasma operational conditions, particularly the plasma operation frequency. An increase in this frequency can trigger reverse chemical processes (formation of N_2 and O_2 from NO_x) and a significant thermal effect. The obtained results also showed that plasma-assisted NF is more energy-demanding in the presence of water, showing an increase in the energy cost (based on plasma-deposited power) by approximately 14 ± 8%. This was associated with energy losses during water evaporation and dissociation. Furthermore, we demonstrated that although the multi-pin plasma system with a liquid electrode suffers from the same drawbacks as a single-pin plasma [29], it allows a drastic increase in the production rate, showing the possible up-scalability and, hence, industrial potential of these plasma systems.

Supplementary Materials: The following supporting information can be downloaded at: https://www.mdpi.com/article/10.3390/app13137619/s1, Figure S1. Electrical circuit of the pulsed plasma generator. Figure S2. Voltage curve as a function of time for a plasma power of 20 W and a gas flow rate of 4 L·min^{-1}. T represents the plasma period. Figure S3. Example of MassiveOES simulation of the OES spectrum of the Me–Me electrode system for a gas flow rate of 4 L min-1 and a discharge power of 90 ± 2 W. Figure S4. Discharge frequency variation in the chopping gap as a function of power for the different flow rates under study in the Me–Me and Me–L systems. Figure S5. Gas temperature as a function of plasma power for the different flow rates under study in the Me–Me and Me–L systems. Figure S6. Estimated electron density as a function of plasma power for the different flow rates under study in the Me–Me and Me–L systems. Figure S7. (a,c) NO and (b,d) NO_2 concentrations as a function of SEI for different gas flow rates for the Me–Me and Me–L systems. Figure S8. Evolution of (a) nitrite and (b) nitrate concentrations generated in the liquid phase as a function of SEI in different gas flow rates for the Me–L system. Figure S9. Energy cost of the pulsed discharge as a function of SEI for different gas flow rates in both electrode configurations. Table S1. Possible chemical reactions occurring in the gas and liquid phases.

Author Contributions: Conceptualization, M.A.S.M., A.N., M.G., Y.G. and N.D.G.; data curation, M.N., A.N., M.G. and Y.G.; formal analysis, M.A.S.M., M.N., M.G., Y.G. and R.B.; funding acquisition, R.M. and N.D.G.; investigation, M.A.S.M. and R.B.; methodology, A.N., M.G. and Y.G.; project administration, N.D.G.; resources, R.M. and N.D.G.; supervision, R.M. and N.D.G.; visualization, M.A.S.M., M.N. and M.G.; writing—original draft, M.A.S.M., M.N., A.N., M.G. and Y.G.; writing—review and editing, M.A.S.M., M.N., A.N., M.G., Y.G., R.M. and N.D.G. All authors have read and agreed to the published version of the manuscript.

Funding: This research was funded by the NITROPLASM FWO-FNRS Excellence of Science (EOS) project (grant 30505023), and the Bio-economy project (grant G0G2322N), funded by the European Union-NextGenerationEU.

Institutional Review Board Statement: Not applicable.

Informed Consent Statement: Not applicable.

Data Availability Statement: Not applicable.

Conflicts of Interest: There are no conflict to declare.

References

1. Zerkle, A.L.; Mikhail, S. The Geobiological Nitrogen Cycle: From Microbes to the Mantle. *Geobiology* **2017**, *15*, 343–352. [CrossRef]
2. Smil, V. Nitrogen and Food Production: Proteins for Human Diets. *Ambio* **2002**, *31*, 126–131. [CrossRef] [PubMed]
3. Bazhenova, T.A.; Shilov, A.E. Nitrogen Fixation in Solution. *Coord. Chem. Rev.* **1995**, *144*, 69–145. [CrossRef]
4. Canfield, D.E.; Glazer, A.N.; Falkowski, P.G. The Evolution and Future of Earth's Nitrogen Cycle. *Science* **2010**, *330*, 192–196. [CrossRef]
5. Galloway, J.N.; Townsend, A.R.; Erisman, J.W.; Bekunda, M.; Cai, Z.; Freney, J.R.; Martinelli, L.A.; Seitzinger, S.P.; Sutton, M.A. Transformation of the Nitrogen Cycle. *Science* **2008**, *320*, 889–892. [CrossRef] [PubMed]
6. Ghavam, S.; Vahdati, M.; Wilson, I.G.; Styring, P. Sustainable ammonia production processes. *Front. Energy Res.* **2021**, *9*, 808. [CrossRef]
7. Smith, C.; Hill, A.K.; Torrente-Murciano, L. Current and Future Role of Haber-Bosch Ammonia in a Carbon-Free Energy Landscape. *Energy Environ. Sci.* **2020**, *13*, 331–344. [CrossRef]
8. Cherkasov, N.; Ibhadon, A.O.; Fitzpatrick, P. A Review of the Existing and Alternative Methods for Greener Ni-trogen Fixation. *Chem. Eng. Process Process Intensif.* **2015**, *90*, 24–33. [CrossRef]
9. Graham, P.H.; Vance, C.P. Nitrogen Fixation in Perspective: An Overview of Research and Extension Needs. *Field Crops Res.* **2000**, *65*, 93–106. [CrossRef]
10. Rusanov, V.D.; Fridman, A.A.; Sholin, G.V. The Physics of a Chemically Active Plasma With Non-equilibrium Vibrational Excitationc of Molecules. *Soviet Physics. Uspekhi* **1981**, *24*, 447–474. [CrossRef]
11. Bogaerts, A.; Neyts, E.C. Plasma Technology: An Emerging Technology for Energy Storage. *ACS Energy Lett.* **2018**, *3*, 1013–1027. [CrossRef]
12. Asisov, R.I.; Givotov, V.K.; Rusanov, V.D.; Fridman, A. High Energy Chemistry (Khimia Vysokikh Energij). *Sov. Phys.* **1980**, *14*, 366.
13. Gatilova, L.V.; Allegraud, K.; Guillon, J.; Ionikh, Y.Z.; Cartry, G.; Röpcke, J.; Rousseau, A. NO Formation Mecha-nisms Studied by Infrared Laser Absorption in a Single Low-Pressure Plasma Pulse. *Plasma Sources Sci. Technol.* **2007**, *16*, S107–S114. [CrossRef]
14. Tsonev, I.; O'Modhrain, C.; Bogaerts, A.; Gorbanev, Y. Nitrogen Fixation by an Arc Plasma at Elevated Pressure to Increase the Energy Efficiency and Production Rate of NO_x. *ACS Sustain. Chem. Eng.* **2023**, *11*, 1888–1897. [CrossRef]

15. Namihira, T.; Katsuki, S.; Hackam, R.; Akiyama, H.; Okamoto, K. Production of nitric oxide using a pulsed arc discharge. *IEEE Trans. Plasma Sci.* **2002**, *30*, 1993–1998. [CrossRef]
16. Wang, W.; Patil, B.; Heijkers, S.; Hessel, V.; Bogaerts, A. Nitrogen Fixation by Gliding Arc Plasma: Better Insight by Chemical Kinetics Modelling. *ChemSusChem* **2017**, *10*, 2145–2157. [CrossRef]
17. Moscosa-santillan, M.; Vincent, A.; Santirso, E.; Amouroux, J. Design of a DBD Wire-Cylinder Reactor for NO x Emission Control: Experimental and Modelling Approach. *J. Clean. Prod.* **2008**, *16*, 198–207. [CrossRef]
18. Krop, J.; Krop, E.; Pollo, I. Calculated Amounts of Nitric Oxide in a Nitrogen-Oxygen Plasma Jet. *Chemi. Plazmy.* **1979**, 242–249.
19. Coudert, J.F.; Baronnet, J.M.; Rakowitz, J.; Fauchais, P. Synthesis of Nitrogen Oxides in a Plasma Produced by a Jet Arc Generator. *Chim. Plasmas.* **1977**, *1*.
20. Patil, B.S.; Wang, Q.; Hessel, V.; Lang, J. Plasma N 2 -Fixation: 1900–2014. *Catal. Today* **2015**, *256*, 49–66. [CrossRef]
21. Xia, P.; Pan, X.; Jiang, S.; Yu, J.; He, B.; Ismail, P.M.; Bai, W.; Yang, J.; Yang, L.; Zhang, H.; et al. Designing a redox heterojunction for photocatalytic "overall nitrogen fixation" under mild conditions. *Adv. Mater.* **2022**, *34*, 2200563. [CrossRef] [PubMed]
22. Barnum, D.W. Some history of nitrates. *J. Chem. Educ.* **2003**, *80*, 1393. [CrossRef]
23. Hollevoet, L.; Vervloessem, E.; Gorbanev, Y.; Nikiforov, A.; De Geyter, N.; Bogaerts, A.; Martens, J.A. Energy-Efficient Small-Scale Ammonia Synthesis Process with Plasma-enabled Nitrogen Oxidation and Catalytic Reduction of Adsorbed NO_x. *ChemSusChem* **2022**, *15*, e202102526. [CrossRef] [PubMed]
24. Li, L.; Tang, C.; Cui, X.; Zheng, Y.; Wang, X.; Xu, H.; Zhang, S.; Shao, T.; Davey, K.; Qiao, S.Z. Efficient nitrogen fixation to ammonia through integration of plasma oxidation with electrocatalytic reduction. *Angew. Chem.* **2021**, *133*, 14250–14256. [CrossRef]
25. Ohneda, H.; Harano, A.; Sadakata, M.; Takarada, T. Improvement of NO_x removal efficiency using atomization of fine droplets into corona discharge. *J. Electrostat.* **2002**, *55*, 321–332. [CrossRef]
26. Shi, J.; Bian, W.; Yin, X. Organic Contaminants Removal by the Technique of Pulsed High-Voltage Discharge in Water. *J. Hazard. Mater.* **2009**, *171*, 924–931. [CrossRef] [PubMed]
27. Vervloessem, E.; Gromov, M.; De Geyter, N.; Bogaerts, A.; Gorbanev, Y.; Nikiforov, A. NH_3 and HNO_x Formation and Loss in Nitrogen Fixation from Air with Water Vapor by Nonequilibrium Plasma. *ACS Sustain. Chem. Eng.* **2023**, *11*, 4289–4298. [CrossRef]
28. Bian, W.; Song, X.; Shi, J.; Yin, X. Nitrogen fixed into HNO_3 by pulsed high voltage discharge. *J. Electrostat.* **2012**, *70*, 317–326. [CrossRef]
29. Gromov, M.; Kamarinopoulou, N.; Geyter, N.; Morent, R.; Snyders, R.; Vlachos, D.; Dimitrakellis, P.; Nikiforov, A. Plasma-Assisted Nitrogen Fixation: The Effect of Water Presence. *Green Chem.* **2022**, *24*, 9677–9689. [CrossRef]
30. Huiskamp, T. Nanosecond Pulsed Streamer Discharges Part I: Generation, Source-Plasma Interaction and Energy-Efficiency Optimization. *Plasma Sources Sci. Technol.* **2020**, *29*, 23002. [CrossRef]
31. Yao, C.; Zhao, Z.; Dong, S.; Zuo, Z. High-Voltage Subnanosecond Pulsed Power Source with Repetitive Frequency Based on Marx Structure. *IEEE Trans. Dielectr. Electr. Insul.* **2015**, *22*, 1896–1901. [CrossRef]
32. Bruggeman, P.J.; Kushner, M.J.; Locke, B.R.; Gardeniers, J.G.; Graham, W.G.; Graves, D.B.; Hofman-Caris, R.C.H.M.; Maric, D.; Reid, J.P.; Ceriani, E.; et al. Plasma–liquid interactions: A review and roadmap. *Plasma Sources Sci. Technol.* **2016**, *25*, 053002. [CrossRef]
33. Voráč, J.; Synek, P.; Potočňáková, L.; Hnilica, J.; Kudrle, V. Batch Processing of Overlapping Molecular Spectra as a Tool for Spatio-Temporal Diagnostics of Power Modulated Microwave Plasma Jet. *Plasma Sources Sci. Technol.* **2017**, *26*, 025010. [CrossRef]
34. Sremački, I.; Gromov, M.; Leys, C.; Morent, R.; Snyders, R.; Nikiforov, A. An atmospheric pressure non-self-sustained glow discharge in between metal/metal and metal/liquid electrodes. *Plasma Process. Polym.* **2020**, *17*, 1900191. [CrossRef]
35. Wu, S.; Cheng, W.; Huang, G.; Wu, F.; Liu, C.; Liu, X.; Zhang, C.; Lu, X. Positive Streamer Corona, Single Filament, Transient Glow, Dc Glow, Spark, and Their Transitions in Atmospheric Air. *Phys. Plasmas* **2018**, *25*, 123507. [CrossRef]
36. Chu, P.K.; Lu, X. (Eds.) *Low Temperature Plasma Technology: Methods and Applications*; CRC Press: Boca Raton, FL, USA, 2013.
37. Nikiforov, A.Y.; Leys, C.; Gonzalez, M.A.; Walsh, J.L. Electron Density Measurement in Atmospheric Pressure Plasma Jets: Stark Broadening of Hydrogenated and Non-Hydrogenated Lines. *Plasma Sources Sci. Technol.* **2015**, *24*, 034007. [CrossRef]
38. Briels, T.M.P.; Kos, J.; Winands, G.J.J.; Van Veldhuizen, E.M.; Ebert, U. Positive and negative streamers in ambient air: Measuring diameter, velocity and dissipated energy. *J. Appl. Phys. D* **2008**, *41*, 234004. [CrossRef]
39. Hagelaar, G.J.M.; Pitchford, L.C. Solving the Boltzmann equation to obtain electron transport coefficients and rate coefficients for fluid models. *Plasma Sources Sci. Technol.* **2005**, *14*, 722–733. [CrossRef]
40. Deng, X.L.; Nikiforov, A.Y.; Vanraes, P.; Leys, C.; Deng, X.L.; Nikiforov, A.Y.; Vanraes, P.; Leys, C. Direct Current Plasma Jet at Atmospheric Pressure Operating in Nitrogen and Air. *J. Appl. Phys.* **2013**, *113*, 023305. [CrossRef]
41. Fox, J.B. Kinetics and Mechanisms of the Griess Reaction. *Anal. Chem.* **1979**, *51*, 1493–1502. [CrossRef]
42. Bruggeman, P.J.; Iza, F.; Brandenburg, R. Fast pulsed discharges. *Plasma Sources Sci. Technol.* **2017**, *26*, 020201.
43. Lin, J.; He, X.; Chen, Q.; Xiong, Q.; Li, J.; Wang, X.; Chen, G.; Liu, Q.H.; Ostrikov, K. The formation mechanism of aqueous hydrogen peroxide in a plasma-liquid system with liquid as the anode. *Eur. Phys. J. D* **2020**, *74*, 80. [CrossRef]
44. Bismo, S.; Chem, J.; Baranova, E.; Irawan, K.; Karamah, E.F.; Saksono, N. On the Production of OH Radical through Plasma Electrolysis Mechanism for the Processing of Ammonia Waste Water. *J. Chem. Chem. Eng.* **2013**, *7*, 6–12.
45. Ono, R.; Teramoto, Y.; Oda, T. Effect of Humidity on Gas Temperature in the Afterglow of Pulsed Positive Corona Discharge. *Plasma Sources Sci. Technol.* **2009**, *19*, 015009. [CrossRef]
46. Bruggeman, P.; Leys, C. Non-Thermal Plasmas in and in Contact with Liquids. *J. Phys. D Appl. Phys.* **2009**, *42*, 053001. [CrossRef]

47. Raizer, Y.P.; Allen, J.E. *Gas Discharge Physics*; Springer: Berlin, Germany, 1991; Volume 1, p. 52.
48. Vanraes, P.; Nikiforov, A.; Bogaerts, A.; Leys, C. Study of an AC dielectric barrier single micro-discharge filament over a water film. *Sci. Rep.* **2018**, *8*, 10919. [CrossRef]
49. Wang, X.; Stockett, P.; Jagannath, R.; Bane, S.; Shashurin, A. Time-resolved measurements of electron density in nanosecond pulsed plasmas using microwave scattering. *Plasma Sources Sci. Technol.* **2018**, *27*, 07LT02. [CrossRef]
50. Vervloessem, E.; Aghaei, M.; Jardali, F.; Hafezkhiabani, N.; Bogaerts, A. Plasma-Based N2Fixation into NOx: In-sights from Modeling toward Optimum Yields and Energy Costs in a Gliding Arc Plasmatron. *ACS Sustain. Chem. Eng.* **2020**, *8*, 9711–9720. [CrossRef]
51. Gromov, M.; Leonova, K.; De Geyter, N.; Morent, R.; Snyders, R.; Britun, N.; Nikiforov, A. N2oxidation Kinetics in a Ns-Pulsed Discharge above a Liquid Electrode. *Plasma Sources Sci. Technol.* **2021**, *30*, 65024. [CrossRef]
52. Gromov, M.; Leonova, K.; Britun, N.; De Geyter, N.; Morent, R.; Snyders, R.; Nikiforov, A. Plasma Nitrogen Fixa-tion in the Presence of a Liquid Interface: Role of OH Radicals. *React. Chem. Eng.* **2022**, *7*, 1047–1052. [CrossRef]
53. Drenck, K.; Hvelplund, P.; Nielsen, S.B.; Panja, S.; Støchkel, K. On the Formation and Fragmentation of Nitrate in Mixed Clusters Using Atmospheric Pressure Corona Discharge in Air. *Int. J. Mass. Spectrom.* **2008**, *273*, 126–131. [CrossRef]
54. He, Z.; Liu, J.; Cai, W. The Important Role of the Hydroxy Ion in Phenol Removal Using Pulsed Corona Discharge. *J. Electrostat.* **2005**, *63*, 371–386. [CrossRef]
55. Lee, J.; Sun, H.; Im, S.; Soo Bak, M. Formation of Nitrogen Oxides from Atmospheric Electrodeless Microwave Plasmas in Nitrogen–Oxygen Mixtures. *J. Appl. Phys.* **2017**, *122*, 083303. [CrossRef]
56. Hao, X.; Mattson, A.M.; Edelblute, C.M.; Malik, M.A.; Heller, L.C.; Kolb, J.F. Nitric Oxide Generation with an Air Operated Non-Thermal Plasma Jet and Associated Microbial Inactivation Mechanisms. *Plasma Process. Polym.* **2014**, *11*, 1044–1056. [CrossRef]
57. Capitelli, M.; Ferreira, C.M.; Gordiets, B.F.; Osipov, A.I. *Plasma Kinetics in Atmospheric Gases*; Springer Science & Business Media: Berlin/Heidelberg, Germany, 2013; Volume 31.
58. Sakakura, T.; Takatsuji, Y.; Morimoto, M.; Haruyama, T. Nitrogen fixation through the plasma/liquid interfacial reaction with controlled conditions of each phase as the reaction locus. *Electrochemistry* **2020**, *88*, 190–194. [CrossRef]
59. Peng, P.; Schiappacasse, C.; Zhou, N.; Addy, M.; Cheng, Y.; Zhang, Y.; Anderson, E.; Chen, D.; Wang, Y.; Liu, Y.; et al. Plasma in situ gas–liquid nitrogen fixation using concentrated high-intensity electric field. *J. Phys. D Appl. Phys.* **2019**, *52*, 494001. [CrossRef]
60. Tarabová, B.; Lukeš, P.; Janda, M.; Hensel, K.; Šikurová, L.; Machala, Z. Specificity of detection methods of nitrites and ozone in aqueous solutions activated by air plasma. *Plasma Process. Polym.* **2018**, *15*, e1800030. [CrossRef]